PAPER

Check for updates

Enhancement of third-order optical nonlinearity of VSe$_2$ by hybridizing with CoSe$_2$ as flower-like nanoparticles†

Marziyeh Parishani, [iD] [a] Marzieh Nadafan [iD] *[b] and Sajad Akbarpoor[b]

Through one-pot hydrothermal synthesis, we synthesized VSe$_2$–CoSe$_2$ nanostructures with a distinctive flower-like morphology. The structural characterizations were conducted using X-ray diffraction (XRD), field emission scanning electron microscopy (FESEM), and Fourier transform infrared spectroscopy (FTIR). By modulating the proportion of the CoSe$_2$ phase, we transformed these hybrid nanostructures into nanoparticles, thereby influencing their nonlinear optical properties. The third-order nonlinear optical parameters (n_2 and β) were rigorously examined *via* the precise Z-scan technique under various laser power conditions. The nanostructures demonstrated a self-focusing refractive response and exhibited pronounced two-photon absorption during the nonlinear absorption process. The magnitudes of n_2 and β were determined to be in the order of 10^{-8} (cm^2 W^{-1}) and 10^{-4} (cm W^{-1}), respectively. The exceptional figure of merit (FOM) of these composite flower-like structures underscores their superior nonlinear optical characteristics, establishing them as promising candidates for photonic applications, particularly in optical switching devices.

1. Introduction

In recent years, the fields of optics and photonics have extensively used transition metal dichalcogenides (TMDCs). The TMDCs have outstanding optical properties and have been widely applied for applications such as optoelectronic devices, energy storage, and energy conversion systems. These properties include high carrier mobility, valley polarization, and fractured symmetry.[1,2]

Materials belonging to this group of materials have a main chemical formula of MX$_2$ (M = W, Mo, V, Zr, *etc.*, and X = S, Se, and Te) with a layered crystal structure. There are TMDCs in several categories, including semiconductor phase (MoS$_2$, *etc.*), superconductors (NbSe$_2$, *etc.*), semimetals (MoTe$_2$, *etc.*), and metal phase (VSe$_2$, *etc.*).[3] VSe$_2$ is a member of TMDs in that the electron delocalization in the vanadium lattice framework is responsible for the high electrical conductivity of vanadium diselenide (VSe$_2$).[4] Many researchers have developed optoelectronic devices using metal TMDCs due to their unique properties, such as fast electron kinetics and charge transport.[5–10] The research on various applications of VSe$_2$-based structures has become prevalent in recent years, especially in metal-ion batteries and energy conversion fields.[11–16]

In the recent three years, the research on nonlinear optical features of VSe$_2$-based materials has developed and there is a clear scientific horizon to achieve an effective nonlinear optical structure in this group of materials due to brilliant optical responses.[10,17–24] Li and coworkers[19] investigated the generation of femtosecond and large-energy mode-locked laser pulses by VSe$_2$ nanosheets that showed great nonlinear optical characteristics. Wang *et al.*[25] showed the high-quality saturation absorption of liquid phase exfoliated VSe$_2$. The saturable absorption properties of VSe$_2$ in the cavity of a D-shaped fiber laser were characterized by Ahmad[26] *et al.* In our study, we achieved competitive results by hybridization of VSe$_2$ and CoSe$_2$ as a distinguished structure to reinforce the nonlinear optical behaviour of the VSe$_2$ structure.

In this study, we synthesized a VSe$_2$–CoSe$_2$ nanocomposite utilizing a straightforward hydrothermal synthesis method. The nanostructures were constructed by varying molar percentages of cobalt. We employed several characterization techniques, including X-ray diffraction (XRD) analysis, field emission scanning electron microscopy (FESEM), and Fourier transform infrared (FTIR) spectroscopy, to assess the microstructural properties. Furthermore, the sensitive Z-scan technique was employed to evaluate the third-order nonlinear optical parameters of the synthesized nanostructures.

[a]Department of Physics, Tarbiat Modares University, P. O. Box 14115-175, Tehran, Iran

[b]Department of Physics, Shahid Rajaee Teacher Training University, P. O. Box 16788-15811, Tehran, Iran. E-mail: m.nadafan@sru.ac.ir; m_naddafan@yahoo.com

† Electronic supplementary information (ESI) available. See DOI: https://doi.org/10.1039/d4ra04192e

2. Materials and method

2.1. Characterization techniques

The XRD data were collected using the D8-Advance device from Bruker AXS that was equipped with a CuK$_\alpha$ tube. A DRS S_4100

SCINCO instrument was used to record the data of UV-visible spectroscopy. The captured field emission electron microscopic images (FESEM) were recorded on a FE-SEM MIRA3 TESCAN electron microscopy device. Raman Spectroscopy was performed on a TEKSAN P50C0R10 instrument and the Fourier transform infrared spectra were recorded on a Thermo AVATAR apparatus.

2.2. Materials

Ammonium metavanadate (NH_4VO_3, 99%), sodium bromide ($NaBH_4$), selenium powder, and cobalt(II) chloride ($CoCl_2 \cdot 6H_2O$) were purchased from Sigma-Aldrich Co.

2.3. Synthesis of CoSe$_2$–VSe$_2$

We prepared the hybrid nanostructure of vanadium diselenide and cobalt selenide *via* a simple hydrothermal route. In the first step, the proper quantity of Se powder and $NaBH_4$ precursors were dissolved in the aqua solution. We utilized sodium bromide powder to incorporate the pure selenium powder into subsequent chemical reactions. In this step, we had a dark red solution. Then, the addition of ammonium metavanadate to the solution converted the transparent liquid to a black and homogenous solution after a while.

In the next step, a proper amount of cobalt precursor was added to the above solution, and we obtained a homogenous black solution after 2 hours. There is an important point for choosing the molar ratio of the precursors.

To synthesize pure VSe$_2$, the molar ratios of vanadium to selenium and $NaBH_4$ precursors were maintained at 1 : 2 and 1 : 4, respectively. For the incorporation of the cobalt precursor, 0.05, 0.1, and 0.2 moles were subtracted from the total amount of the vanadium precursor and replaced with the corresponding amounts of the cobalt precursor. The resultant homogeneous dark solution was transferred to a sealed autoclave container, where the chemical reaction was conducted at 200 °C for 24 hours. Upon cooling to room temperature, the black precipitate was washed with deionized water and absolute ethanol using a paper filter, followed by drying in a furnace at 80 °C overnight. The prepared samples, differentiated by the varying amounts of cobalt precursor, were labeled as VC1, VC2, and VC3, corresponding to $x = 0.05$, 0.1, and 0.2 moles of the Co precursor, respectively.

3. Results and discussion

3.1. XRD analysis

Fig. 1 represents the XRD analysis results of the as-prepared samples employed to determine their crystallographic patterns. The main peaks of the VSe$_2$ structure were observed at 29.75° and 43.7° related to the (002) and (102) crystal planes and they match with those from the reference card JCPDS no.89-1641. Also, the peaks related to the CoSe$_2$ structure were observed at 51.8° and 56.2° related to (311) and (023) crystal planes, respectively. The intensity and width of each peak altered and it is an obvious outcome due to the construction of hybrid structures, increasing the percentage of Co into the
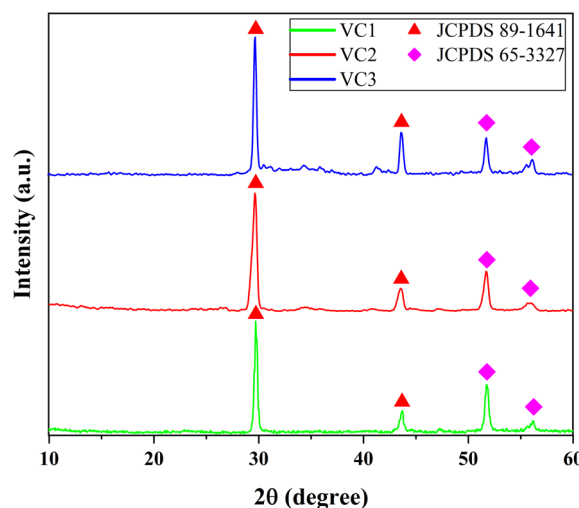

Fig. 1 XDR patterns of the samples.

whole compound and the change in the size of hybrid structures.

3.2. FE-SEM image analysis

The morphologies of various prepared nanostructures were characterized from FESEM images as shown in Fig. 2. The
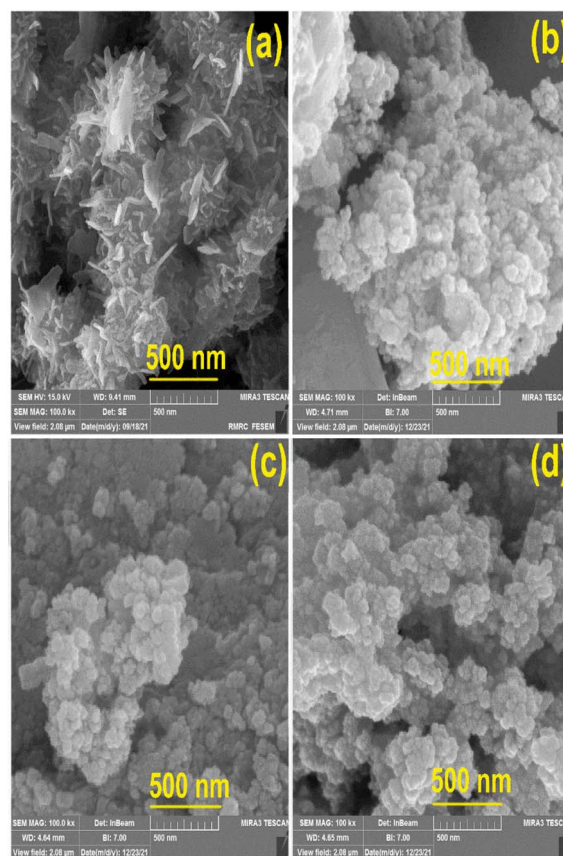

Fig. 2 SEM micrographs of (a) VSe$_2$, (b) VC1 (c) VC2, and (d) VC3.

morphology of pure VSe$_2$ is sheet structure while the morphology changes to nanoparticles upon adding different amounts of the cobalt precursor during the preparing step of the materials. The mean thickness of the VSe$_2$ sheet structure was measured at 16 nm and the particle sizes of VC1, VC2, and VC3 samples were estimated as 29.1, 43.45, and 32 (nm), respectively.

It is noteworthy that the VSe$_2$ nanosheet serves as an effective substrate for the growth of CoSe$_2$ nanostructures, resulting in a morphological transformation from a nanosheet to a flower-like nanostructure. This alteration in particle size indicates that the optimal amount of the Co precursor to be added to the VSe$_2$ structure is 20 percent of the total amount of the vanadium precursor. Specifically, this proportion of the Co precursor leads to a size reduction compared to pure VSe$_2$, while exceeding this value results in an increase in size.

Most importantly, the presence of CoSe$_2$ nanostructures on VSe$_2$ nanosheets inevitably affects the shape of such structure and therefore the formation of CoSe$_2$ nanoparticles dominates the VSe$_2$ sheets by increasing the amount of the Co counterpart. In addition, as a result of the exciting magnetic properties of Co-based structures, they tend to attract metal ions and bond, and ultimately, this can impress the particle size.

Among the aforementioned reasons, the size distribution of each structure including sheet thickness and particle size (Fig. 3) indicated that the average thickness of VSe$_2$ nanosheets is 12.5 nm and the mean particle sizes for each flower-like structure of VSe$_2$–CoSe$_2$ composition are approximately 38, 35, and 27 (nm), respectively. It is obvious that the distribution of the particle size has a downward trend and the minimum value is related to a sample with 20% Co precursor.

3.3. Diffuse reflectance spectroscopy (DRS)

To assess the optical features and the bandgap energy of all nanohybrid structures, we measured the diffuse reflectance spectroscopy that illustrates the reflection responses of the materials in the UV-visible region. A key parameter, called Kubelka–Mank (K–M) function $F(R_\infty)$, helps evaluate the energy of band gap, E_g. The K–M function is defined as $(1 - R_\infty)2/2R_\infty$ and R_∞ is the diffuse reflection data we observed from DRS spectra. The depiction of $(F(R_\infty)h\nu)^2$ versus energy wavelength ($h\nu$) (Fig. S1†) is a powerful method to estimate the E_g of nanostructures. It is a straightforward tool and E_g can be determined by extrapolation of the linear part of the plot. The average value of band gap energy is 4.38, 4.58, 4.7, and 4.68 (eV) for VSe$_2$, VC1, VC2, and VC3 samples, respectively.

3.4. Raman Spectroscopy

For the evaluation of the optical vibrational modes and verification of the VSe$_2$–CoSe$_2$ hybrid formation, we analyzed the Raman modes of nanostructured samples, as shown in Fig. 4. The Raman active modes related to the 1T-phase VSe$_2$ structure were seen at 134 and 229 (cm^{-1}). Raman shifts are assigned to E$_g$ (in-plane) and A$_{1g}$ (out-of-plane), respectively. Also, the vibrational modes at around 446, 510, and 670 (cm^{-1}) Raman shifts are assigned to the CoSe$_2$ structure. The difference between all spectra is that the modes shift to lower or higher Raman shift because of the entrance of Co–Se chemical bonding among the pristine VSe$_2$ structures.

3.5. Fourier transform infrared (FTIR) spectroscopy

The further endorsement of the formation of vital chemical bonds was distinguished via FTIR spectroscopy. As each chemical bond is assigned to a particular vibrational mode in FTIR spectra, the active infrared vibrational modes of Co–Se bonds attributed to CoSe$_2$ structure were demonstrated in the range of 500 (cm^{-1}) to 900 (cm^{-1}) wavenumbers, and the observed FTIR modes between 900–1400 (cm^{-1}) belong to V–Se bonds of VSe$_2$ chemical structures (see Fig. S2†).

4. Nonlinear optical features: Z-scan analysis

An effective and versatile technique for simultaneously measuring the sign and magnitude of nonlinear optical
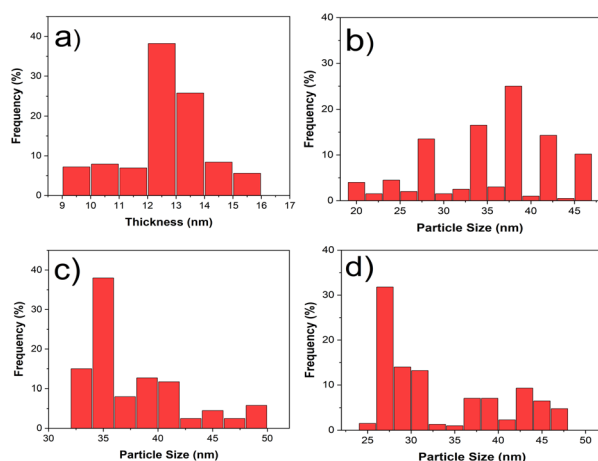

Fig. 3 Histogram plot of particle size distribution: (a) VSe$_2$, (b) VC1, (c) VC2, and (d) VC3.
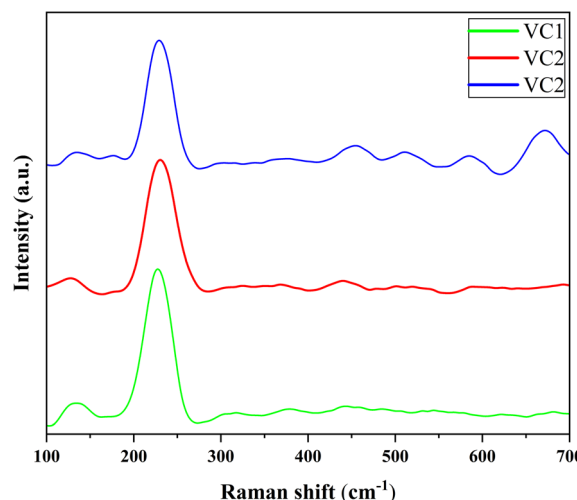

Fig. 4 Raman spectra of the samples.

coefficients is the Z-scan method. The sample was illuminated by a horizontal linear polarized Gaussian CW Nd:YAG laser at the wavelength of 532 nm with the specific power that propagates and focuses through a lens (f = 19 cm). The recording conditions for all samples were the same. As samples were moved during scanning, they were moved at 1 mm intervals.

Using a small aperture in front of the detector (lose-aperture data or CA) or without an aperture (open-aperture data or OA), the transmitted beam amplitude and phase are measured according to the sample position in the z-direction relative to the focal plane, in order to resolve the nonlinear refraction (means NLR) index and nonlinear absorption (or NLA) coefficient. All samples were investigated for this purpose.

This setup was equipped with a detector to measure the intensity of the transmitted laser beam. The intensities of the incident light and the input power of the laser beam were stabilized to guarantee accurate results. The input power of the continuous wave (CW) laser was altered from 30 to 50 mW at 10 mW intervals. The explanation of each section of the Z-scan setup is illustrated in Fig. S3† and the evaluation of the β parameter, NLA coefficient, can be evaluated from the OA Z-scan results according to the eqn (1):

$$\beta = \frac{2\sqrt{2}(1 - T(z))}{I_0 L_{\text{eff}}} \left(1 + \frac{z^2}{z_0^2}\right) \tag{1}$$

In which the effective thickness is $L_{\text{eff}} = [(1 - \exp(-\alpha L))/\alpha]$, the initial value of laser intensity is I_0, and the Rayleigh length is $z_0 = \pi\omega_0^2/\lambda$. $T(z)$ also denotes the normalized transmittance at $z = 0$. The linear absorption formula is $\alpha = -\ln(-P/P_0)/L$ where input and output values of the laser power are P_0 and P, respectively. In other words, these are the values of laser power when the sample is placed within the laser path or not, respectively.

The nonlinearity in the optical properties of materials typically arises from various phenomena, including saturable absorption (SA), multiphoton absorption, reverse saturable absorption (RSA), and free-carrier absorption. The latter phenomenon is associated with the femtosecond timescale.

The dependence of nonlinear optical (NLO) responses on the incident power of the pump laser was meticulously measured for different VSe₂–CoSe₂ nanostructures. As depicted in Fig. 5, which illustrates the intensity-dependent open-aperture (OA) responses of the samples, the focus position corresponded to the minimum value of the beam energy concentration. This observation revealed a symmetry reduction of absorption towards the edges of the butterfly shape. The final results were analyzed at various laser intensities along the z-direction, providing a comprehensive understanding of the NLO behaviour of these nanostructures.

Based on the OA Z-scan data, we calculated β values as shown in Table 3. Additionally, the enhancement of the OA Z-scan data highly depends on input laser intensity. We verified the accuracy of experimental NLA findings through the fitting of solid lines containing theoretical data evaluated by eqn (2) and (3):
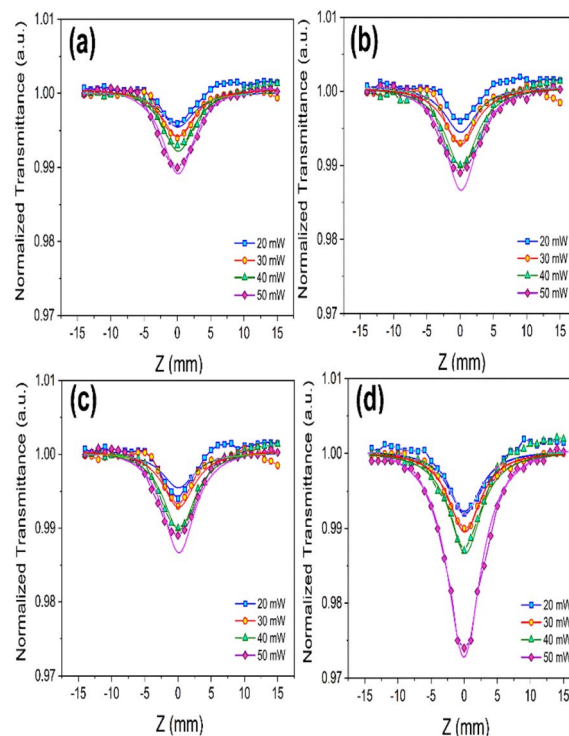

Fig. 5 OA curves of (a) Pure VSe₂, (b) 5%, (c) 10%, and (d) 20% Co of VSe₂–CoSe₂ nanostructures, at different incident power of the laser.

$$T_{\text{norm}}(z) = \sum_{m=0}^{\infty} \frac{[-q_0(z,0)]^m}{(m+1)^{3/2}} \tag{2}$$

$$q_0(z,t) = (\beta I_0 L_{\text{eff}})/(1 + z^2/z_0^2) \tag{3}$$

where I_0 and L_{eff} are identified as the initial intensity of the employed laser and effective path length into the sample. The experimental data of the open-aperture Z-scan associated with the nonlinear essence of the samples can be related to the two-photon process of absorption or 2PA.

The CA Z-scan data showed a peak-valley configuration for transmittance, explaining a positive NLR value that identifies the self-focusing responses of the nonlinear refractive feature of samples. Based on eqn (4), the difference between peak and valley of transmittance, T_{P-V}, is assigned to a particular phase parameter $\Delta\varphi_0$ that is the on-axis alteration of such a factor:

$$\Delta T_{P-V} = 0.406(1 - S)^{0.25}|\Delta\varphi_0| \\ \Delta\varphi_0 = (2\pi/\lambda)n_2 I_0 L_{\text{eff}} \tag{4}$$

In the aforementioned equation, the linear transmittance expression for the aperture is attributed to the linear transmittance parameter, S, while the n_2 coefficient defines the nonlinear refractive (NLR) factor. As illustrated in Fig. 6, the NLR coefficient increased with the enhancement of laser intensity. The strong correlation between the experimental values (scattered points) and the theoretical results (solid line) was validated by Sheik-Bahae. Eqn (5) represents the data matching process for the experimental closed-aperture (CA) results:
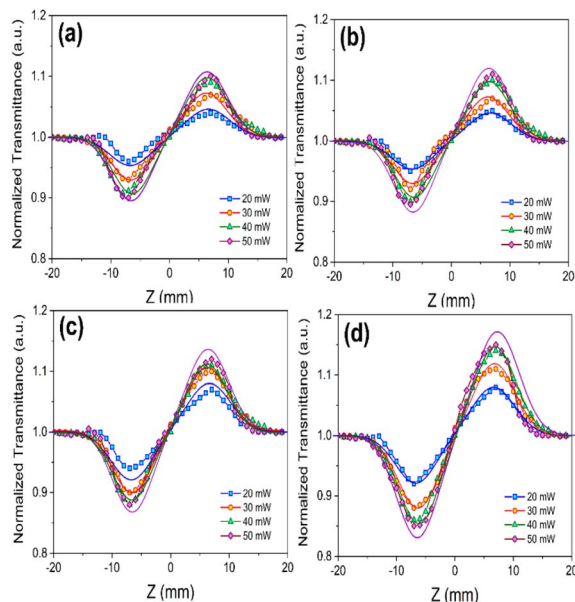
Fig. 6 CA curves of (a) VSe_2 pure, (b) 5%, (c) 10%, and (d) 20% Co precursor in VSe_2–$CoSe_2$ nanostructures, at different incident power of the laser.

$$T_{norm} = 1 - \frac{4x\Delta\varphi_0}{(1+x^2)(9+x^2)}; \; x = \frac{z}{z_0} \quad (5)$$

where the diffraction length parameter of the light source is Z_0. The NLR index and NLA coefficient of samples were in the orders of 10^{-8} (cm^2 W^{-1}) and 10^{-4} (cm W^{-1}), respectively. The NLO coefficients of the synthesized samples are given in Table 1.

The maximum magnitudes for the nonlinear refractive index (n_2) and the nonlinear absorption coefficient (β) of the VSe_2–$CoSe_2$ nanostructures, corresponding to 20% Co in VSe_2, were determined to be 4.11×10^{-8} cm^2 W^{-1} and 2.47×10^{-4} cm W^{-1}, respectively. Our Z-scan analysis revealed that self-focusing behaviour and the two-photon absorption (2PA) process are the primary nonlinear optical phenomena observed in our transition metal dichalcogenide (TMD) nanostructures.

Nonlinear dispersion and local heating at each point of the sample, resulting from the temperature dependence of the refractive index, along with the absorption behaviour of the excited levels in species involved, contribute to the nonlinearities observed in Z-scan spectra. The use of a continuous wave (CW) laser source emphasizes the roles of these latter two factors. Such investigations and measurements can provide valuable evaluations of the nonlinear optical (NLO) parameters and enhance corresponding optical applications. The fundamental mechanisms of nonlinear absorption in transition metal dichalcogenide (TMD) species generally include saturable absorption (SA), reverse saturable absorption (RSA), and two-photon absorption (2PA). RSA and 2PA increase the absorption process, while SA decreases absorption by increasing the irradiance intensity of the laser source.

The significant results of the 2PA phenomenon in our Z-scan study can be exclusively discussed by the fundamental concept of the 5-level electron transition when it comes to CW laser irradiance. First and foremost, the intersystem movement (ISM) plays a vitally important role in the case of CW laser interaction. As Shown in Fig. S4†, electrons transit from the ground level S_0 to the first excited level S_1 and then back to the first triplet level T_1. These electronic transitions are taken into account as ISM. Secondly, the transition from level T_1 to T_2 is expected and such electronic transfers can play a significant role in 2PA responses in the case of CW laser irradiation. In other words, the cross-section area belonging to triplet transfers can hugely support the possibility of the 2PA phenomenon in this area.[27,28]

The second important cause of optical nonlinearity in this study is indicated as thermal lensing effects. Generally, as far as CW lasers are employed, the refractive coefficient is a function of temperature (T), as defined $n(r,t) = n_0 + (dn/dt) \Delta T(r,t)$, where n_0 is the linear part of total refractive index. In the optical environment, the interaction of light beams and molecules of materials may lead to induce local heat in the medium. The radial increasing temperature may be conducive to an alterable heat field that is not a linear function of the localized light intensity of the laser source.[29–32]

Table 1 Nonlinear coefficients of VSe_2–$CoSe_2$ hybrid nanostructures under CW laser excitation at 532 nm by the Z-scan method

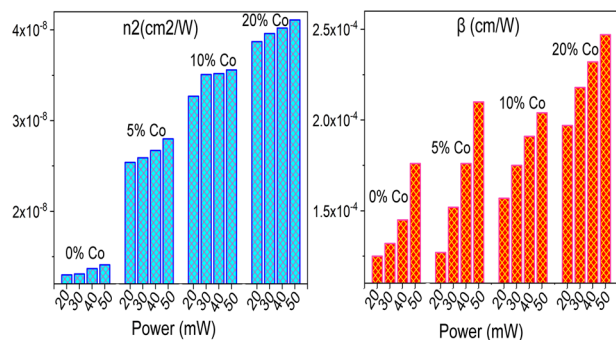| Sample	P_{in} (mW)	α (cm^{-1})	ΔT	ω_0 (μm)	I_0 (W cm^{-2})	n_2 (cm^2 W^{-1}) $\times 10^{-8}$	β (cm W^{-1}) $\times 10^{-4}$
0% Co	20	2.87	0.05	3.5	1039.91	1.30	1.25
	30	2.74	0.08	3.6	1474.40	1.31	1.32
	40	2.48	0.09	3.8	1764.39	1.37	1.45
	50	2.35	0.10	4.2	1805.40	1.41	1.76
5% Co	20	3.19	0.10	3.5	1039.91	2.54	1.27
	30	2.46	0.15	3.6	1474.40	2.59	1.52
	40	1.91	0.19	3.8	1764.39	2.67	1.76
	50	2.27	0.20	4.2	1805.40	2.80	2.10
10% Co	20	2.92	0.13	3.5	1039.91	3.27	1.57
	30	2.67	0.20	3.6	1474.40	3.51	1.75
	40	3.56	0.23	3.8	1764.39	3.52	1.91
	50	3.42	0.24	4.2	1805.40	3.56	2.04
20% Co	20	2.12	0.16	3.5	1039.91	3.87	1.97
	30	2.32	0.23	3.6	1474.40	3.96	2.18
	40	2.35	0.28	3.8	1764.39	4.04	2.32
	50	2.42	0.29	4.2	1805.40	4.11	2.47

Fig. 7 Alteration trend of n_2 and β among various prepared VSe$_2$–CoSe$_2$ flower-like nanostructures.

Furthermore, the hybridization of CoSe$_2$ in VSe$_2$ can enhance the NLO features because the metal ions increase the charge transfer states. In fact, when metal centers are pushed or pulled by electrons, novel charge transfer states lead to higher NLO responses. Therefore, it is expected that the nonlinear optical responses of VSe$_2$–CoSe$_2$ hybrid nanostructures are higher than those of VSe$_2$ nanosheets. The explanation of the significant change of nonlinear optical coefficients compared to that of pure VSe$_2$ sample is illustrated in charts of Fig. 7 and an increasing trend is seen in all composite nanostructures.

The effect of increasing laser power on the nonlinear optical (NLO) parameters is inferred from the number of incident photons per surface area. As laser intensity is defined by $I = P$ (watt)/A (A being the area of the irradiated surface), an increase in the power of the light beam results in a higher number of incident photons interacting with the optical materials. When the number of absorbed photons is enhanced, the intensity of all NLO responses and the number of excited electrons increase. Consequently, the NLO coefficients are significantly impacted and improved. Furthermore, an increase in the intensity of the electromagnetic wave field leads to a higher number of polarized molecules in the absorber medium, ultimately resulting in an enhancement of the nonlinear refractive index.

Several studies have reported similar reasons for the improvement of nonlinear optical (NLO) responses in transition metal dichalcogenides (TMDs), as summarized in Table 3. Kumar and his coworkers documented the exceptional ultrafast optical performance of SWCNT-VSe$_2$, attributing the enhancement of NLO properties to the strong donor–acceptor electron correlation, which plays a crucial role in augmenting the optical material's NLO attributes.[18] They demonstrated that low saturation light intensity and significant modulation depth facilitate the realization of ultrashort pulse output in microfiber-based few-layer V$_2$CT$_x$. The VSe$_2$–CoSe$_2$ flower-like nanostructures exhibit superior NLO responses compared to other well-known structures such as WTe$_2$, MoTe$_2$, and WS$_2$.[33–36] These findings suggest that the VSe$_2$–CoSe$_2$ nanostructure is a highly promising candidate for applications in optical switching, mode locking, Q-switching, optical limiting, and optoelectronic devices.

Other nonlinear optical factors include third-order nonlinear optical susceptibility that is evaluated from previous nonlinear optical coefficients including n_2 and β. These equations for each part of this parameter (real and imaginary parts) are as follows:

$$\mathrm{Re}\left[\chi^{(3)}\right](\mathrm{esu}) = 10^{-4}\frac{\varepsilon_0 c^2 n_0^2}{\pi}n_2\left(\mathrm{cm}^2\ \mathrm{W}^{-1}\right) \quad (6)$$

$$\mathrm{Im}\left[\chi^{(3)}\right](\mathrm{esu}) = 10^{-2}\frac{\varepsilon_0 c^2 n_0\lambda}{4\pi^2}\beta\left(\mathrm{cm}\ \mathrm{W}^{-1}\right) \quad (7)$$

Interestingly, the linear refractive coefficient (n_0) can be estimated by this eqn (8), which considers a broad range of materials with a high band gap:[37]

$$n_0 = \sqrt{\frac{A}{E_g^{0.5}} - B}; \begin{cases} A = (3.44)^2 \\ B = \sqrt{3.44} \end{cases} \quad (8)$$

In fact, the evaluation of band gap energy (E_g) was investigated in the DRS results and this is 4.38, 4.58, 4.7, and 4.68 (eV) for

Table 2 Evaluation of main parameters in optical switching for samples

Sample	n_0	P_0 (mW)	Re($\chi^{(3)}$) × 10^{-6} (esu)	Im($\chi^{(3)}$) × 10^{-8} (esu)	$\chi^{(3)}$ × 10^{-6} (esu)	FOM
0% Co	1.949	20	1.252	2.617	1.25	1.95
		30	1.262	2.764	1.26	1.86
		40	1.320	3.036	1.32	1.77
		50	1.358	3.685	1.35	1.50
5% Co	1.916	20	2.365	2.613	2.36	3.75
		30	2.411	3.128	2.41	3.20
		40	2.486	3.622	2.48	2.85
		50	2.607	4.321	2.60	2.50
10% Co	1.898	20	2.988	3.201	2.98	3.91
		30	3.207	3.568	3.20	3.77
		40	3.216	3.894	3.21	3.46
		50	3.253	4.159	3.25	3.28
20% Co	1.901	20	3.547	4.022	3.54	3.69
		30	3.630	4.451	3.63	3.41
		40	3.703	4.737	3.70	3.27
		50	3.767	5.043	3.76	3.12

Table 3 Nonlinear optical properties of similar components in comparison with VSe$_2$–CoSe$_2$ hybrid nanostructures

Materials	λ (nm)	$n_2 \times 10^{-8}$ (cm^2 W^{-1})	$\beta \times 10^{-3}$ (cm W^{-1})	SDF/SF[a]	TPA/SA/RSA[a]	Ref.
MoSe$_2$–PMMA	632.8	-6.76×10^{-7}	4.68×10^{-8}	SDF	SA	41
WSe$_2$	532	10^{-10}	—	—	—	42
PEDOT:PSS/MoSe$_2$	633	7.73×10^{-7}	6.86×10^{-8}	SF	SA	43
MoS$_2$/PVA	633	10^{-7}	10^{-6}	SDF	SA	44
VSe$_2$	532	6.99	0.5		TPA	This work
VSe$_2$–CoSe$_2$(5% Co)	532	2.86	0.35		TPA	This work
VSe$_2$–CoSe$_2$(10% Co)	532	3.56	0.204		TPA	This work
VSe$_2$–CoSe$_2$(20% Co)	532	4.11	0.256		TPA	This work

[a] The abbreviation words including SF, SDF, TPA, SA, and RSA are denoted as self-focusing, self-defocusing, two-photon absorption, saturable absorber, and reverse saturable absorber, respectively.

pure VSe$_2$, VC1, VC2, and VC3 samples, respectively. Clearly, the $\chi^{(3)}$ for all samples rises significantly as a result of increasing previous nonlinear optical parameters and increasing the rate of laser power.

One of the prevalent applications of nonlinear optical materials is in optical switches and this valuable potential of such materials is assessed *via* the figure of merit factor or FOM of materials. FOM is an optical parameter related to both the imaginary part of $\chi^{(3)}$ and the linear absorption of materials, as expressed in the following formula:

$$FOM = n_2/\lambda\beta \qquad (9)$$

When this parameter is above 1, it is an essential criterion for optical switches;[38–40] therefore, as seen in Table 2, this can be implicated that such transition metal dichalcogenide composition (VSe$_2$–CoSe$_2$) possesses superior performance for optical switching applications.

5. Conclusions

In this research, the hydrothermal process for synthesizing VSe$_2$/CoSe$_2$ nanostructures proceeded by opting for various amounts of CoSe$_2$ phases. The variation of size distribution for all samples was analyzed based on the CoSe$_2$ phase concentration. Thus, the optical properties of both linear and nonlinear values were altered under the above conditions.

Based on the valuable results of Z-scan spectra analysis, the magnitude of β coefficient is in the order of 10^{-4} (cm W^{-1}) and the two-photon absorption process dominates all other nonlinear absorption processes. Additionally, the nonlinear n_2 index is in the order of 10^{-8} (cm^2 W^{-1}) and the dominant nonlinear optical behaviour was the self-focusing response.

The enhancement of NLO parameters with increasing laser power suggests a rise in local thermal phenomena and two-photon absorption (2PA) processes during NLO interactions, thereby supporting the use of these structures in optical switching devices. The superior performance of such hybrid TMDs is evidenced by a FOM greater than 1, surpassing other well-known TMDs. The comparison of the NLO behaviours of VSe$_2$–CoSe$_2$ nanostructures underscores their excellent potential for future photonic and optical applications and research.

Data availability

The data supporting this article have been included as part of the ESI.†

Author contributions

Marziyeh Parishani and Marzieh Nadafan contributed to concepts, material synthesis, data analysis, writing and reviewing of all content of this article. Marzieh Nadafan was also the supervisor of this project. Sajad Akbarpoor contributed to the data analysis in this study.

Conflicts of interest

There are no conflicts to declare.

Acknowledgements

References

1 Z. Sun, H. Chu, Y. Li, L. Liu, S. Zhao, G. Li and D. Li, *Opt. Mater. Express*, 2019, **9**, 3494–3503.
2 Q. Cao, F. F. Yun, L. Sang, F. Xiang, G. Liu and X. Wang, *Nanotechnology*, 2017, **28**, 475703.
3 G. Liu, S. Dai, B. Zhu, P. Li, Z. Wu and Y. Gu, *Opt. Laser Technol.*, 2019, **120**, 105746.
4 J. Feng, D. Biswas, A. Rajan, M. D. Watson, F. Mazzola, O. J. Clark, K. Underwood, I. Markovic, M. McLaren and A. Hunter, *Nano Lett.*, 2018, **18**, 4493–4499.
5 G. Duvjir, B. K. Choi, I. Jang, S. Ulstrup, S. Kang, T. Thi Ly, S. Kim, Y. H. Choi, C. Jozwiak and A. Bostwick, *Nano Lett.*, 2018, **18**, 5432–5438.
6 Q. Zhu, M. Shao, S. H. Yu, X. Wang, Z. Tang, B. Chen, H. Cheng, Z. Lu, D. Chua and H. Pan, *ACS Appl. Energy Mater.*, 2018, **2**, 644–653.
7 Y. Bai, H. Zhang, B. Xiang, X. Liang, J. Hao, C. Zhu and L. Yan, *ACS Appl. Mater. Interfaces*, 2021, **13**, 23230–23238.

8 H. Ci, J. Cai, H. Ma, Z. Shi, G. Cui, M. Wang, J. Jin, N. Wei, C. Lu and W. Zhao, *ACS Nano*, 2020, **14**, 11929–11938.

9 C. Yang, J. Feng, F. Lv, J. Zhou, C. Lin, K. Wang, Y. Zhang, Y. Yang, W. Wang and J. Li, *Adv. Mater.*, 2018, **30**, 1800036.

10 J. Zhang, H. Chen, M. Zhang, H. Yuan, J. Yin, J. Wang and P. Yan, in *2019 18th International Conference on Optical Communications and Networks (ICOCN)*, IEEE, 2019, pp. 1–4.

11 Z. Wu, C. Lu, Y. Wang, L. Zhang, L. Jiang, W. Tian, C. Cai, Q. Gu, Z. Sun and L. Hu, *Small*, 2020, **16**, 2000698.

12 F. Ming, H. Liang, Y. Lei, W. Zhang and H. N. Alshareef, *Nano Energy*, 2018, **53**, 11–16.

13 M. Alahmadi, M. Farrag, E. El-Dok, M. A. Moselhy and E. Sheha, *Mater. Lett.*, 2023, **341**, 134300.

14 L. Najafi, R. Oropesa-Nuñez, S. Bellani, B. Martín-García, L. Pasquale, M. Serri, F. Drago, J. Luxa, Z. Sofer and D. Sedmidubský, *ACS Nano*, 2021, **16**, 351–367.

15 S. Raj KA, P. Mane, S. Radhakrishnan, B. Chakraborty and C. S. Rout, *ACS Appl. Nano Mater.*, 2022, **5**, 4423–4436.

16 I. S. Kwon, I. H. Kwak, G. M. Zewdie, S. J. Lee, J. Y. Kim, S. J. Yoo, J.-G. Kim, J. Park and H. S. Kang, *ACS Nano*, 2022, **16**, 12569–12579.

17 V. Kumar, S. R. K. A. Afreen, P. Mane, B. Chakraborty, C. S. Rout and K. V Adarsh, *J. Phys. Chem. C*, 2023, **127**, 18485–18493.

18 V. Kumar, D. Mandal, K. A. S. Raj, B. Chakraborty, A. Agarwal, C. S. Rout and K. V Adarsh, *Phys. Rev. Appl.*, 2023, **19**, 44081.

19 L. Li, L. Pang, Q. Zhao, W. Liu and Y. Su, *J. Mater. Chem. C*, 2020, **8**, 1104–1109.

20 V. Kumar, K. A. Raj, C. S. Rout and K. V Adarsh, *AIP Conf. Proc.*, 2024, **2995**, 1.

21 J. Huang and Y. Tang, *Infrared Phys. Technol.*, 2024, 105182.

22 B. Wang, H. Han, L. Yu, Y. Wang and C. Dai, *Nanophotonics*, 2021, **11**, 129–137.

23 X. Li, Y. Zhang, Y. Zhao, X. Shi, T. Feng and K. Zhang, *Ann. Phys.*, 2021, **533**, 2100230.

24 N. Li, J. Huang, L. Du, L. Yang, J. Li, D. Liu, L. Miao and C. Zhao, *Opt. Express*, 2022, **30**, 6838–6845.

25 T. Wang, X. Shi, J. Wang, Y. Xu, J. Chen, Z. Dong, M. Jiang, P. Ma, R. Su and Y. Ma, *Sci. China Inf. Sci.*, 2019, **62**, 1–8.

26 H. Ahmad, N. A. M. Ariffin, S. N. Aidit, S. I. Ooi, N. Yusoff and A. K. Zamzuri, *Optik*, 2021, **230**, 166280.

27 U. Tripathy and P. B. Bisht, *J. Opt. Soc. Am. B*, 2007, **24**, 2147–2156.

28 M. Abdullah, H. Bakhtiar, G. Krishnan, M. S. A. Aziz, W. H. Danial and S. Islam, *Opt. Laser Technol.*, 2019, **115**, 97–103.

29 M. Saravanan, S. G. TC and G. Vinitha, *J. Mol. Liq.*, 2018, **256**, 519–526.

30 N. Priyadarshani, G. Vinitha and T. C. S. Girisun, *Opt. Laser Technol.*, 2018, **108**, 287–294.

31 G. Muruganandi, M. Saravanan, G. Vinitha, M. B. J. Raj and T. C. S. Girisun, *Opt. Mater.*, 2018, **75**, 612–618.

32 C. Babeela, T. C. S. Girisun and G. Vinitha, *J. Phys. D Appl. Phys.*, 2015, **48**, 65102.

33 H. Pan, H. Chu, Y. Li, S. Zhao and D. Li, *J. Alloys Compd.*, 2019, **806**, 52–57.

34 V. Ramar, P. M. Pataniya, S. Gunvant and B. Karthikeyan, *J. Appl. Phys.*, 2022, **132**, 10.

35 M. Yan, L. Chai, Q. Song, W. Liu and M. Hu, *Opt. Mater.*, 2020, **107**, 110040.

36 C. Quan, M. He, C. He, Y. Huang, L. Zhu, Z. Yao, X. Xu, C. Lu and X. Xu, *Appl. Surf. Sci.*, 2018, **457**, 115–120.

37 H. M. Gomaa, I. S. Yahia and H. Y. Zahran, *Phys. B*, 2021, **620**, 413246.

38 Q. Li, X. Yuan, X. Jiang, J. Wang, Y. Liu and L. Zhang, *RSC Adv.*, 2021, **11**, 32446–32453.

39 A. S. Asyikin, A. A. Latif, M. K. Halimah, M. H. M. Zaid, M. A. Kamarudin, M. F. Fazzny, S. N. Nazrin and I. Zaitizila, *Opt. Laser Technol.*, 2024, **168**, 109857.

40 M. F. Fazzny, M. K. Halimah, C. Eevon, A. A. Latif, F. D. Muhammad, A. S. Asyikin, S. N. Nazrin and I. Zaitizila, *Opt. Laser Technol.*, 2020, **127**, 106161.

41 R. Kaur, K. P. Singh and S. K. Tripathi, *J. Mater. Sci. Mater. Electron.*, 2020, **31**, 19974–19988.

42 Y. Jia, Y. Shan, L. Wu, X. Dai, D. Fan and Y. Xiang, *Photon. Res.*, 2018, **6**, 1040–1047.

43 R. Kaur, K. P. Singh and S. K. Tripathi, in *AIP Conference Proceedings*, AIP Publishing, 2020, vol. 2220.

44 K. Anand, R. Kaur, A. Arora and S. K. Tripathi, *Opt. Mater.*, 2023, **137**, 113523.